



## Spatial mapping of greenhouse gases using a UAV monitoring platform over a megacity in China

Tianran Han<sup>a,1</sup>, Conghui Xie<sup>a,1</sup>, Yanrong Yang<sup>a</sup>, Yuheng Zhang<sup>a</sup>, Yufei Huang<sup>a</sup>, Yayong Liu<sup>a</sup>, Keyu Chen<sup>a</sup>, Haijiong Sun<sup>a</sup>, Jietao Zhou<sup>a</sup>, Chang Liu<sup>a</sup>, Junfei Guo<sup>b</sup>, Zhijun Wu<sup>a</sup>, Shao-Meng Li<sup>a,\*</sup>

<sup>a</sup> State Key Joint Laboratory of Environmental Simulation and Pollution Control, College of Environmental Sciences and Engineering, Peking University, Beijing 100871, PR China

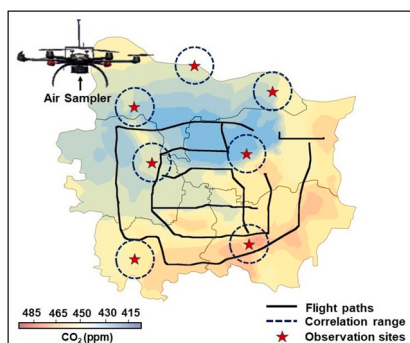
<sup>b</sup> Beijing Wisdominc Technology Co., Ltd., Beijing 100070, PR China



### HIGHLIGHTS

- CO<sub>2</sub> and CH<sub>4</sub> mixing ratios were mapped using a UAV platform over a megacity in China.
- The spatial correlation range for both CO<sub>2</sub> and CH<sub>4</sub> in the urban area is approximately 2 km.
- Urban GHG monitoring network designed for emission inversion purposes can have a minimal spatial resolution of 4 km.

### GRAPHICAL ABSTRACT



### ARTICLE INFO

Editor: Jianmin Chen

#### Keywords:

Greenhouse gases  
Methane  
Carbon dioxide  
UAV measurements  
Spatial autocorrelation  
GHG monitoring network

### ABSTRACT

Urban environments are recognized as main anthropogenic contributors to greenhouse gas (GHG) emissions, characterized by unevenly distributed emission sources over the urban environments. However, spatial GHG distributions in urban regions are typically obtained through monitoring at only a limited number of locations, or through model studies, which can lead to incomplete insights into the heterogeneity in the spatial distribution of GHGs. To address such information gap and to evaluate the spatial representation of a planned GHG monitoring network, a custom-developed atmospheric sampler was deployed on a UAV platform in this study to map the CO<sub>2</sub> and CH<sub>4</sub> mixing ratios in the atmosphere over Zhengzhou in central China, a megacity of nearly 13 million people. The aerial survey was conducted along the main roads at an altitude of 150 m above ground, covering a total distance of 170 km from the city center to the suburbs. The spatial distributions of CO<sub>2</sub> and CH<sub>4</sub> mixing ratios in Zhengzhou exhibited distinct heterogeneities, with average mixing ratios of CO<sub>2</sub> and CH<sub>4</sub> at 439.2 ± 10.8 ppm and 2.12 ± 0.04 ppm, respectively. A spatial autocorrelation analysis was performed on the measured GHG mixing ratios across the city, revealing a spatial correlation range of approximately 2 km for both CO<sub>2</sub> and

\* Corresponding author.

E-mail address: [shaomeng.li@pku.edu.cn](mailto:shaomeng.li@pku.edu.cn) (S.-M. Li).

<sup>1</sup> Contributed equally to this work.

$\text{CH}_4$  in the urban area. Such a spatial autocorrelation distance suggests that the urban GHG monitoring network designed for emission inversion purposes need to have a spatial resolution of 4 km to characterize the spatial heterogeneities in the GHGs. This UAV-based measurement approach demonstrates its capability to monitor GHG mixing ratios across urban landscapes, providing valuable insights for GHG monitoring network design.

## 1. Introduction

Atmospheric carbon dioxide ( $\text{CO}_2$ ) and methane ( $\text{CH}_4$ ) are the two most important anthropogenic greenhouse gases (GHGs) with significant implications for climate change. Global atmospheric  $\text{CH}_4$  mixing ratios have risen by 2.6-fold from 722 ppb in pre-industrial times to 1908 ppb by 2022. The current global atmospheric  $\text{CO}_2$  mixing ratio is about 1.5 times higher than pre-industrial levels (~278 ppm) and continues to increase steadily (Lan et al., 2024). GHG levels are rising due to carbon emissions from both natural processes and human activities, with fossil fuel combustion being the main contributor (IPCC, 2022). Long-term monitoring networks have been established worldwide, mostly in remote locations, to gain a comprehensive understanding of the temporal variations in atmospheric GHG levels, which indicate global carbon cycle dynamics and emissions. Prominent global carbon monitoring networks are included in the Global Atmospheric Watch Program of the World Meteorological Organization (WMO/GAW), such as that operated by the Earth System Research Laboratory of the National Oceanic and Atmospheric Administration (NOAA/ESRL). These networks primarily focus on monitoring sites located in remote areas with few human activities to accurately depict the long-term mixing ratio trends and source/sink characteristics in the background or large-scale regions (Lee et al., 2018). More recent urban networks, such as BEACO<sub>2</sub>N, are designed primarily for the purpose of GHG emission inversion (Turner et al., 2020), as well as capturing the urban spatial distribution of GHGs. Such an urban network design requires a more comprehensive approach to capture the impact of anthropogenic sources and localized emissions.

Urban areas are major contributors to GHG emissions, driven by high energy use in transportation, heating/cooling, domestic consumption as well as construction and industrial activities. In fact, more than 80 % of global anthropogenic GHG emissions comes from urban areas worldwide (George et al., 2007). This scenario is expected to be similar in China, where urbanization and industrialization have experienced remarkable acceleration in recent decades. As of 2022, China's urbanization rate was 64.7 % and is expected to reach 75–80 % by 2035 (South China Morning Post, 2022). Urban atmospheric GHG mixing ratios are a result of complex interplay between emissions, urban landscape and meteorological conditions (Defratyka et al., 2021). Mapping and analyzing  $\text{CO}_2$  and  $\text{CH}_4$  levels in urban atmospheres enable a better understanding of the spatial distribution and variability of GHG sources within these environments. Such mapping provides valuable insights into the localized impacts of emissions and can serve as the *priori* source distributions in emission inversion modeling (Chan et al., 2020; Jackson et al., 2020).

A detailed mapping of GHG levels in urban atmosphere can also serve as a guidance for urban monitoring network design. Near-surface mixing ratios of  $\text{CO}_2$  and  $\text{CH}_4$  have been extensively studied and documented through elevated point measurements at monitoring stations in major cities worldwide, including Phoenix (Balling Jr et al., 2001; Idso et al., 2001), Baltimore (George et al., 2007), the San Francisco Bay Area (Turner et al., 2020) in the U.S., Rome (Gratani and Varone, 2005) in Italy, Essen (Henninger and Kuttler, 2010) in Germany, and Shanghai (Liu et al., 2019) and Xi'an (Wang et al., 2021) in China. However, while point measurements offer valuable temporal resolution, their spatial coverage remains limited (Büns and Kuttler, 2012). The scarcity of monitoring stations in cities, along with the heterogeneity of urban GHG sources and the complexity of urban environments, makes it difficult to constrain spatial variations in GHG mixing ratios in urban atmosphere. Ground mobile observations of GHG in cities partially fill such a data gap

on a campaign basis, providing finer spatial resolutions and covering different land-use types (Mitchell et al., 2018; Sun et al., 2019). For example, Defratyka et al. (2021) used vehicle-based mobile measurements of  $\text{CH}_4$  in Paris to provide data on street-level concentrations of  $\text{CH}_4$ , and identified and quantified emission sources. Mallia et al. (2020) mapped  $\text{CO}_2$  concentrations and constrained  $\text{CO}_2$  emissions in Salt Lake City, Utah using measurements made from a light rail public transit platform. However, in Zhengzhou, China, the study region for this research, only elevated point measurements of daily variations in GHG mixing ratios have been reported (Shi et al., 2013). While such ground-based mobile measurements offer improved spatial distribution of GHG mixing ratios along the driving routes, they are constrained by route accessibility and might experience disturbances from nearby sources, in particular traffic emissions, that can affect the representativeness of the collected data. No systematic evaluation of the representativeness of ground monitoring stations and mobile measurements of GHG in cities has been reported. To address such an issue, unmanned aerial vehicles (UAVs) can fly above urban obstacles like buildings and vegetation, making them suitable platforms from which to conduct more precise representative measurements of urban GHG and allowing an evaluation of the spatial representation of measurements and providing guidance to monitoring network design.

UAVs have emerged as valuable platforms for atmospheric measurements since the beginning of the 21st century (Villa et al., 2016). Compared to other mobile platforms, UAVs are more flexible, versatile, and cost-effective (Allen et al., 2019; Golston et al., 2018). UAVs can be launched from and land at random locations, hover in mid-air, operate at low airspeeds, and fly complex flight plans (Barchyn et al., 2017; Han et al., 2024). In addition, UAVs can operate at altitudes lower than 200 m where manned aircrafts are unable to reach, thereby meeting the need for near-surface GHG mixing ratio measurements (Mayer et al., 2010). Despite these advantages associated with their use, the integration of UAVs with instruments for mapping GHG mixing ratios has remained largely unexplored, especially over urban regions. UAV flights in urban areas can be restricted by aviation safety regulations and typically needs air traffic controller (ATC) approval before flight. As a result, deployment of UAVs for mapping GHG mixing ratios in urban environments has yet to reach the full potentials of such airborne measurement platforms.

In this study, an innovative integrated UAV system was developed to monitor GHG mixing ratios within an urban environment. To the best of our knowledge, this is the first time that such an UAV system was deployed for GHG mapping over a megacity. Throughout June 2022, a series of UAV-based measurement campaigns were conducted along the main ring roads of Zhengzhou City, China. The measured GHG mixing ratios over the city were analyzed for spatial autocorrelation, and a kriging interpolation approach was used to predict  $\text{CO}_2$  and  $\text{CH}_4$  at unobserved locations, providing wider spatial coverage across the city. By effectively capturing the spatial autocorrelation of GHG mixing ratios, this study aimed to gain insights into the minimal spatial resolution requirement of measurements for monitoring across the urban landscape, and to validate the spatial representativeness of the long term GHG monitoring stations in Zhengzhou. Consequently, this work improves the understanding of the siting criteria for the GHG monitoring network in the city's urban area. Such insights play an important role in assisting policy makers in making informed decisions and developing effective climate mitigation policies.

## 2. Method

### 2.1. Study area

Zhengzhou is one of China's largest cities, situated on the southern bank of the Yellow River. According to the 2020 Chinese census, Zhengzhou covers an area of 7446 km<sup>2</sup> and is home to a population of 12.6 millions. Zhengzhou is approximately 110 m above sea level. As the capital city of Henan Province, Zhengzhou is the political, economic and technological hub of the province. Additionally, located in north-central region of China, Zhengzhou serves as a pivotal hub for China's national transportation network. Natural gas accounts for approximately 15 % of Zhengzhou's energy consumption. At the peak of the heating season, the daily natural gas consumption in the city exceeds 11 million m<sup>3</sup>. In 2020, there were a total of 75 operational sewage treatment plants in Zhengzhou, with a total capacity of 3.4 million m<sup>3</sup>/d. Additionally, total wetland area inside Zhengzhou is 1052.7 km<sup>2</sup>, including the Yellow River Wetland Reserve which is one of the major river wetlands in central China.

To conduct long-term monitoring of CO<sub>2</sub> and CH<sub>4</sub> mixing ratios in the city, seven GHG observation sites were strategically located across Zhengzhou's various subregions (marked with yellow triangles as shown in Fig. 1). The placement of these sites was determined by the degree of urbanization in each region, with the goal of representing GHG levels in the downtown, commercial, and suburban areas of the city. The present investigation focuses on five districts of Zhengzhou: Huiji, Jinshui, Guancheng, Erqi, and Zhongyuan. These districts are home to significant populations, with Huiji having a population of 0.56 million, Jinshui 1.6 million, Guancheng 0.82 million, Erqi 1.1 million, and Zhongyuan 0.96 million.

### 2.2. UAV measurements

Measurements of the CO<sub>2</sub> and CH<sub>4</sub> mole fractions were made using an integrated UAV sampling platform. An air sampler developed in-house and a 3D sonic anemometer were mounted on the UAV (Fig. 2). Further details concerning the UAV measurement technique can be found in Han et al. (2024) and Yang et al. (2024b).

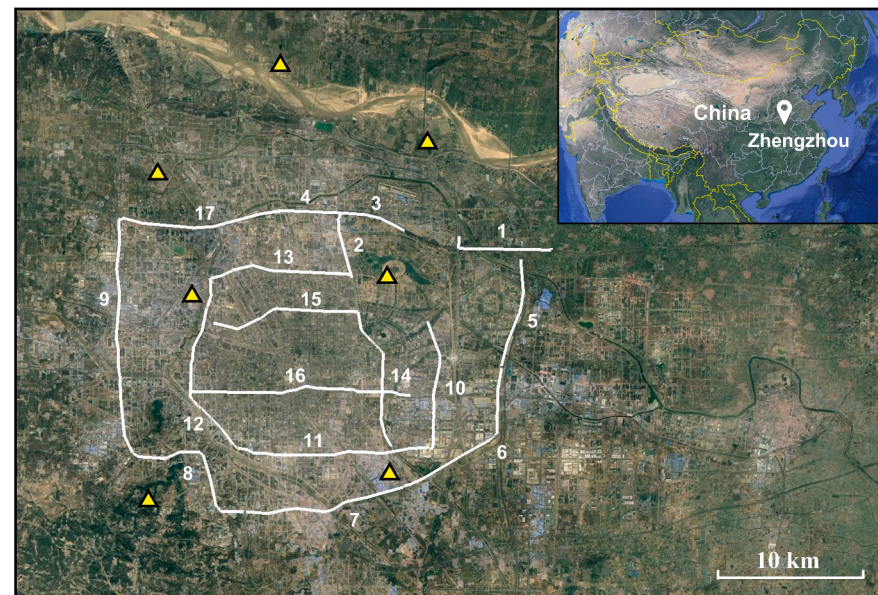


**Fig. 1.** The numbered flight tracks of the UAV spatial survey in the main urban areas of Zhengzhou City. The start time (Beijing Time, GMT + 8:00), end time (GMT + 8:00), and the total distance for each flight are listed in the table to the right. The locations of the GHG observation sites were marked with yellow triangles on the map.

### 2.2.1. The UAV

The hexacopter (KWT-X6L-15) has a maximum flight time of ~30 min at a maximum payload of 15 kg. The UAV weighs about 22.5 kg with two batteries loaded. It is capable of flying under wind speeds up to 14.4 m/s to an altitude of about 4000 m and has a maximum horizontal flying speed of 18 m/s, a maximum ascending speed of 4 m/s and a maximum descending speed of 3 m/s. The horizontal precision of the GPS on the UAV during hovering is ±2 m and the vertical precision is ±1.5 m.

### 2.2.2. The air sampler

The air sampler consists of a 150 m thin-walled stainless-steel tubing, a pump, a micro-orifice, a CO<sub>2</sub> marker generator, two three-way solenoid valves and electronic relays, with the electrical devices powered by a lithium battery (Fig. 2(b)). The tubing is wound into a multilayer coil, in whose center the system control components are mounted. The system is housed in a custom-designed highly compact carbon fiber assembly of 280 mm diameter and 98 mm height, that can be mounted at the bottom of the UAV. The gas intake is mounted at 45 cm above the center of gravity of the UAV, placed nearby a sonic anemometer for ensuring sampling the same air where wind speed is measured. The time stamps of the observations are corrected for a time lag of 4 s between the air intake and the stainless-steel tubing. Shortly before every flight, the pump is remotely turned on to sample the CO<sub>2</sub> marker for 5 s to mark the beginning of the flight, and then to collect air samples. During flight, the pump would alternatively sample the marker and the ambient air on a preset timing schedule. The sampling flow rate remains at 18 ccm during the entire flight, controlled with the micro-orifice which is placed between the pump and the coiled tube. After landing, the pump is remotely turned off and the air sample in the tubing is immediately analyzed with a cavity ring-down spectroscopy (CRDS) analyzer (Picarro, Inc., CA, USA, model G2401). The flow rate of the sample from the tubing to the CRDS analyzer is maintained at ~ 54 sccm, 3 times the sampling flow rate. Additional dilution zero air is added to the sample flow to the CRDS analyzer. CO<sub>2</sub> and CH<sub>4</sub> mixing ratios in the sampled air were then obtained. Using the embedded and timed CO<sub>2</sub> marker data, the CO<sub>2</sub> and CH<sub>4</sub> data series can be mapped to the sampling times and GPS locations during flight.

Flight No.	Distance	Start time	End time
1	7.3 km	18:53 22 Jun.	19:16 22 Jun.
2	4.2 km	07:21 23 Jun.	07:46 23 Jun.
3	5.0 km	08:35 23 Jun.	09:05 23 Jun.
4	4.8 km	10:04 23 Jun.	10:30 23 Jun.
5	7.4 km	18:50 23 Jun.	19:15 23 Jun.
6	11.3 km	20:06 23 Jun.	20:32 23 Jun.
7	10.8 km	10:12 24 Jun.	10:38 24 Jun.
8	15.8 km	12:02 24 Jun.	12:30 24 Jun.
9	10.7 km	13:43 24 Jun.	14:09 24 Jun.
10	9.8 km	10:10 25 Jun.	10:50 25 Jun.
11	12.6 km	12:12 25 Jun.	12:37 25 Jun.
12	10.4 km	16:01 25 Jun.	16:20 25 Jun.
13	11.8 km	18:13 25 Jun.	18:43 25 Jun.
14	8 km	09:12 26 Jun.	09:39 26 Jun.
15	12.3 km	10:46 26 Jun.	11:11 26 Jun.
16	16.2 km	14:28 26 Jun.	14:59 26 Jun.
17	11.1 km	16:38 26 Jun.	17:00 26 Jun.

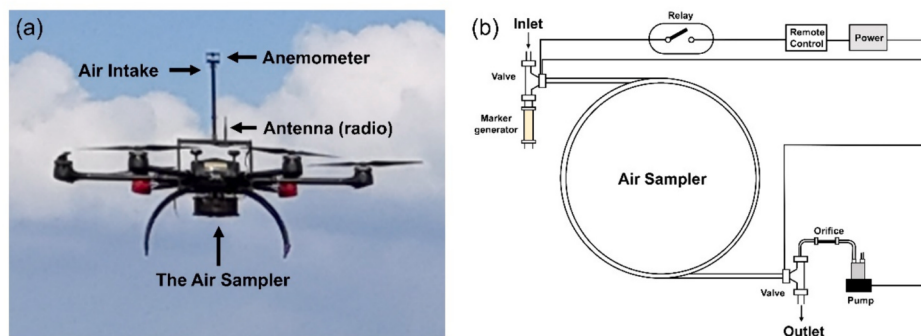


**Fig. 2.** (a) The UAV sampling system. (b) Design of the air sampler.

### 2.2.3. The 3D sonic anemometer

Instead of obtaining meteorological data from ground weather stations to aid data interpretation, a 3D sonic anemometer (Geotech Inc., Denver, US, model Trisonica Mini) is attached on the top of the hexacopter via a 450 mm carbon fiber pole to measure in situ meteorological data including wind speed and direction. The specific positioning of the anemometer on the UAV aims to minimize interfering airflows from the rotors, as determined from flow field computational fluid dynamic simulations (Yang et al., 2024a). This anemometer is capable of measuring wind speeds within the range of 0 to 50 m/s, with an accuracy of  $\pm 0.1$  m/s for speeds below 10 m/s. The wind direction measurement accuracy is  $\pm 1^\circ$ . It measures air temperature within a range of  $-40^\circ\text{C}$  to  $85^\circ\text{C}$  with an accuracy of  $\pm 2^\circ\text{C}$ . Throughout the flight, meteorological data, including wind speed, wind direction, and temperature, are transmitted in real time via a radio antenna at a rate of 3 Hz and collected on the ground. To ensure accurate results, the data undergo post-flight corrections for rotor-induced air flows, true air speeds of the UAV, and changes in UAV flight attitude. These corrections enable the derivation of accurate wind speed and direction data along the flight track (Yang et al., 2024a).

### 2.2.4. UAV flights

A total of 17 UAV flights were conducted from 22 to 26 June 2022 to determine the mixing ratio levels of CO<sub>2</sub> and CH<sub>4</sub> and their spatial distributions over Zhengzhou. These flights covered the central urban region up to the fourth ring road, encompassing both the city's inner and outer areas. The aerial surveys were conducted along the main roads at an altitude of 150 m above ground, covering a total distance of 170 km, as shown in Fig. 1. The UAV was flown at the lowest safe altitude to avoid potential risks from buildings. Vertical distributions may reflect a combination of mixing and emissions, and that mixing ratios from measurements at 150 m may be linked to the near surface mixing ratios under well mixed conditions. Indeed, vertical profiles from the UAV flight during ascent show that the difference in GHG mixing ratios between 150 m and 2 m above the ground is not significant, with the CO<sub>2</sub> levels varying within 4 ppm and CH<sub>4</sub> levels within 0.1 ppm, probably because of a well-mixed boundary layer during the study. Therefore, it is assumed that the GHG mixing ratios observed at 150 m above the ground can represent the heterogeneity of near-surface GHG emissions under our study conditions. Limited by battery capacity, each individual UAV flight was restricted to a maximum range of 18 km. To ensure safety and unobstructed visual sighting, the UAV was flown along the city's primary ring roads, avoiding tall buildings, followed by the mission control vehicle on the ground driving along the roads. For safety measures, before each flight, potential take-off and landing locations were identified and confirmed through on-site assessments. Just before take-off, the predetermined flight paths were reevaluated from a second vehicle to confirm the absence of traffic congestion and other safety concerns along the flight tracks, like flying kites and power lines. Throughout the 17 flights, the UAV maintained straight flight paths,

which included 7 flights covering longitudinal paths and 10 flights covering latitudinal paths. The UAV was flown consistently at speeds between 10 and 12 m/s. The samples collected in the air sampler were measured by the CRDS analyzer at 1 Hz, therefore the spatial resolution for the UAV measurements is 10–12 m (Han et al., 2024). The duration of each flight lasted from 20 to 35 min, and the actual distance covered varied between 4.2 and 16.2 km. This variability was dependent on factors such as available take-off and landing sites and the remaining battery capacity of the UAV.

### 2.3. Data correction

To ensure accurate interpretation of the data, corrections to the data were made to account for daily fluctuations in the UAV measurements. The levels of atmospheric CO<sub>2</sub> and CH<sub>4</sub> vary throughout the day due to human activities and weather conditions, such as temperature and changes in the boundary layer of the atmosphere (Metya et al., 2021). The CO<sub>2</sub> fluctuations at ground level are also influenced by natural processes such as vegetation photosynthesis and respiration (Haszpra et al., 2008). Similar variation patterns have been noticed in other urban areas, including Shanghai (Wei et al., 2020), Delhi (Sahay and Ghosh, 2012), and Florence (Venturi et al., 2020), where both CO<sub>2</sub> and CH<sub>4</sub> mixing ratios at ground are highest in the early morning, decrease around midday, and gradually rise again in the afternoon. The morning peak is attributed to a shallow boundary layer, especially when there's a temperature inversion, and rush-hour traffic emissions in the case of CO<sub>2</sub>. The midday decreases in both CO<sub>2</sub> and CH<sub>4</sub> result from solar-driven convective mixing, CO<sub>2</sub>-uptake due to vegetation photosynthesis, and CH<sub>4</sub> reactions with OH radicals (Sahay and Ghosh, 2012). Consequently, in order to align the data for further analysis, CO<sub>2</sub> and CH<sub>4</sub> mixing ratios measured at different times of the day were normalized to a single time point (7:00 am, Beijing Time) using the daily CO<sub>2</sub>/CH<sub>4</sub> variations observed in Zhengzhou (Shi et al., 2013) or other Chinese cities (Ye et al., 2024). The previous measurements of CO<sub>2</sub> and CH<sub>4</sub> mixing ratios in Zhengzhou were conducted at 1.5 m above ground at the Henan Academy of Agricultural Sciences, near the center of the city and the results were based on the average of a two-year measurement. The normalization process involves obtaining the CO<sub>2</sub> and CH<sub>4</sub> mixing ratios at each hour of the day from the previously observed CO<sub>2</sub> and CH<sub>4</sub> daily variation (Shi et al., 2013; Ye et al., 2024). Then the ratio between the CO<sub>2</sub>/CH<sub>4</sub> mixing ratios at 7:00 am and at each measured time point is calculated based on the daily variation data. This ratio was then applied to the UAV-measured CO<sub>2</sub> and CH<sub>4</sub> data in this study, thus scaling all the measurements to the reference time of 7:00 am:

$$\text{CO}_2_{\text{normalized}}(t) = \frac{\text{CO}_2_{\text{reported}}(7:00 \text{ am})}{\text{CO}_2_{\text{reported}}(t)} \times \text{CO}_2(t) \quad (1)$$

$$\text{CH}_4_{\text{normalized}}(t) = \frac{\text{CH}_4_{\text{reported}}(7:00 \text{ am})}{\text{CH}_4_{\text{reported}}(t)} \times \text{CH}_4(t) \quad (2)$$

where  $CO_2_{normalized}(t)$  and  $CH_4_{normalized}(t)$  represent the normalized  $CO_2$  and  $CH_4$  mixing ratios at time  $t$ ,  $CO_2(t)$  and  $CH_4(t)$  represent the  $CO_2$  and  $CH_4$  mixing ratios measured by the UAV at time  $t$ .  $CO_2_{reported}(t)$  and  $CH_4_{reported}(t)$  represent the previously reported  $CO_2$  and  $CH_4$  mixing ratios at time  $t$  and  $CO_2_{reported}(7:00\ am)$  and  $CH_4_{reported}(7:00\ am)$  the previously reported  $CO_2$  and  $CH_4$  mixing ratios measured at 7:00 am at ground level (Shi et al., 2013).

#### 2.4. Spatial autocorrelation analysis

In order to analyze the degrees of similarity between GHG mixing ratios at different locations within urban area, a spatial autocorrelation analysis was applied to the data. Autocorrelation is the correlation of a time (or space) series with a delayed (or spatially shifted) copy of itself as a function of time lag (or space distance in the case of spatial data series). Given measurements,  $Y_1, Y_2, \dots, Y_N$  at time (or spatial) coordinates  $X_1, X_2, \dots, X_N$ , the lag  $k$  autocorrelation function  $r_k$  is defined as

$$r_k = \frac{\sum_{i=1}^{N-k} (Y_i - \bar{Y})(Y_{i+k} - \bar{Y})}{\sum_{i=1}^N (Y_i - \bar{Y})^2} \quad (3)$$

where the subscript  $i$  represents time sequence or spatial sequential coordinate. Even though the autocorrelation formula doesn't directly involve the distance variable in the case of spatial data series, it does imply that the observations are uniformly spaced for the spatial autocorrelation analyses.

#### 2.5. Kriging interpolation

Due to time constraints and limitations in available road options, the number of measurements that could be taken was restricted. As a result, to achieve a more comprehensive spatial resolution mapping of the distribution of  $CO_2$  and  $CH_4$  levels across Zhengzhou, data interpolation became necessary. Kriging is a commonly used geostatistical technique for interpolation (Ha et al., 2014). The main principle behind kriging is the spatial relationship between attribute values on a geographic surface. Closer pairs of values tend to exhibit stronger correlations compared to those that are farther apart. By incorporating the spatial correlation of observed values based on the semivariogram of the spatial data, Kriging effectively characterizes the spatial relationships among observed values based on their distances from one another. This differentiates Kriging from other interpolation methods like the inverse distance weighted method, as it considers not only the distances between the unknown location and sample locations but also the distances among the sample locations themselves. This aspect helps mitigate the potential impact of clustered samples on the accuracy of the interpolated estimates (Ha et al., 2014). While Kriging has been extensively employed in the study of stationary and time-invariant environmental contaminates such as heavy metal (Ha et al., 2014) in soil and groundwater quality (Belkhiri et al., 2020), its application in the atmospheric environment, where the pollutant levels tend to vary with time, has also been reported, such as  $PM_{2.5}$  (Sampson et al., 2013),  $NO_2$  (van Zoest et al., 2019) and  $CO_2$  (He et al., 2020).

##### 2.5.1. Variogram

Variogram model determines the kriging weights that are used to predict the unknown values at the location of interest. A variogram is mathematically defined as the measure of semi-variance as a function of distance (Belkhiri et al., 2020),

$$\gamma(h) = \frac{1}{2N(h)} \sum_{i=1}^{N(h)} [z(x_i) - z(x_i + h)]^2 \quad (4)$$

where  $\gamma(h)$  is the semi-variance;  $N(h)$  the number of pairs separated by

distance or lag  $h$ ;  $z(x_i)$  the measured sample at point  $x_i$ ; and  $z(x_i + h)$  the measured sample at point  $(x_i + h)$ . The spatial structure of the collected samples is determined by fitting a variogram model to the semi-variance values computed from the data. These variogram models offer insights into the spatial correlation structure and provide essential parameters for the subsequent kriging interpolation process. The input variogram parameters include the range, sill, and nugget.

##### 2.5.2. Ordinary kriging

Ordinary kriging, which is the most commonly employed kriging method, enables the estimation of a value at a specific point within a given region, utilizing data from the surrounding vicinity, given that a variogram is available. The ordinary kriging equation is expressed as (Belkhiri et al., 2020):

$$\hat{Z}(x_p) = \sum_{i=1}^n \lambda_i Z(x_i) \quad (5)$$

In order to achieve unbiased estimations in obtaining appropriate weights  $\lambda_i$  for kriging, the following equation needs to be solved:

$$\sum_{i=1}^n \lambda_i \gamma(x_i, x_p) - \mu = \gamma(x_i, x_p) \text{ where } j = 1, \dots, n \text{ with } \sum_{i=1}^n \lambda_i = 1 \quad (6)$$

where  $\hat{Z}(x_p)$  is the estimated value of variable  $Z$  at location  $x_p$ ;  $Z(x_i)$  is the known value at location  $x_i$ ;  $\lambda_i$  is the weight associated with the data;  $\mu$  is the Lagrange coefficient;  $\gamma(x_i, x_j)$  is the value of variogram corresponding to a vector with origin in  $x_i$  and extremity in  $x_j$ ; and  $n$  is the number of data points used in the estimation.

### 3. Results

#### 3.1. Spatial distribution

The spatial variations in  $CO_2$  and  $CH_4$  mixing ratios across different locations during the monitoring period are shown in Fig. 3, showing the overlay of  $CO_2$  and  $CH_4$  mixing ratios on the map of Zhengzhou of various land use types such as vegetation, water bodies, residential areas, commercial zones, industrial sites, and roads. A consistent pattern is seen from the spatial distributions of  $CO_2$  and  $CH_4$  that higher levels of both gases are observed in the southern and eastern parts of the city, whereas lower levels are found in the northern and western regions. The mixing ratios of  $CO_2$  and  $CH_4$  ranged from 412 to 509 ppm and 2.06 to 2.55 ppm during the survey, with the average of  $CO_2$  and  $CH_4$  at  $439.2 \pm 10.8$  ppm and  $2.12 \pm 0.04$  ppm respectively. The highest  $CH_4$  mixing ratio (2.55 ppm) was spotted during the 16th flight along Longhai Road in the central western area of Zhengzhou. This high level was situated close to a compressed natural gas (CNG) filling station. Similarly, the highest  $CO_2$  mixing ratio of 509 ppm in this study was also observed at a nearby spot, and likely resulted from vehicle fuel combustion near a railway station. Moreover, a  $CO_2$  hotspot was captured in the suburban southeastern part of the city. This region is characterized by a high-density industrial park hosting energy-intensive industries like steel mills, glass manufacturing, hardware production, and automobile manufacturing. These industries apparently contribute to the higher levels of  $CO_2$  in the atmosphere observed in this specific area.

The  $\Delta CH_4$  to  $\Delta CO_2$  ratio can reveal information about the local emission sources. Over a city, this ratio might indicate aspects of its energy infrastructure, level of urbanization, and typical industrial activities. A reduced major axis regression analysis (Davis and Sampson, 1986) was conducted to determine the  $\Delta CH_4$  to  $\Delta CO_2$  ratio. As  $CO_2$  and  $CH_4$  mixing ratios are of very different magnitudes, they were normalized before applying the regression analysis. Across all flights, the correlation coefficient ( $R$ ) between enhanced levels of  $CO_2$  and  $CH_4$  ( $\Delta CO_2$  and  $\Delta CH_4$ ) from their respective background values was determined to be  $0.36 \pm 0.007$ .

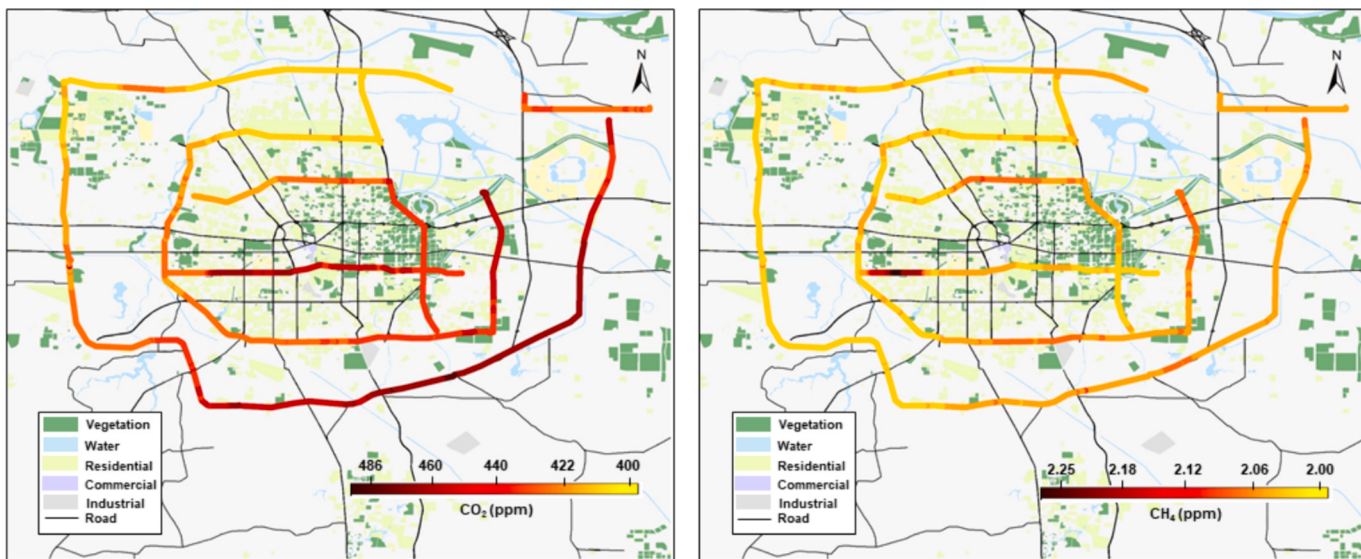


**Fig. 3.** Spatial distributions of CO<sub>2</sub> and CH<sub>4</sub> mixing ratios in Zhengzhou.

It is noteworthy that the red dots in Fig. 4 are apparent outliers from the other data, therefore significantly biasing the correlation coefficient. These outliers correspond to data collected during Flight 16. During this flight, the UAV followed a west-to-east trajectory along the Longhai Road. As the UAV approached the CNG filling station near the Longhai Road, a significant increase in CH<sub>4</sub> mixing ratios was observed, while the corresponding CO<sub>2</sub> mixing ratios remained relatively consistent with background levels (pink triangle dots in Fig. 4). Consequently, on this part of the flight track, the ΔCH<sub>4</sub>/ΔCO<sub>2</sub> ratio was as high as 0.036 ± 0.05. This observation indicates that the high ΔCH<sub>4</sub> might have resulted from fugitive gas leakage or intentional release at the filling station, not from incomplete combustion. Continuing eastward on the same flight, CO<sub>2</sub> was enhanced as the UAV approached a railway station, while CH<sub>4</sub> gradually decreased to background levels (pink round dots in Fig. 4). Subsequently, as the UAV moved away from the two hotspots near the Longhai Road and reached the eastern section, both CH<sub>4</sub> and CO<sub>2</sub> mixing ratios returned to background levels, and the ratio of ΔCH<sub>4</sub>/ΔCO<sub>2</sub> dropped to 0.001 ± 0.0001, which is close to the average value observed throughout the broader city area. After excluding the apparent outliers, the correlation coefficient between ΔCO<sub>2</sub> and ΔCH<sub>4</sub> increased to 0.45 ± 0.006, and the regression slope (ΔCH<sub>4</sub>/ΔCO<sub>2</sub>) was 0.0008 ± 0.1. This value is comparable in magnitude to the ΔCH<sub>4</sub>/ΔCO<sub>2</sub> ratio (0.0003)

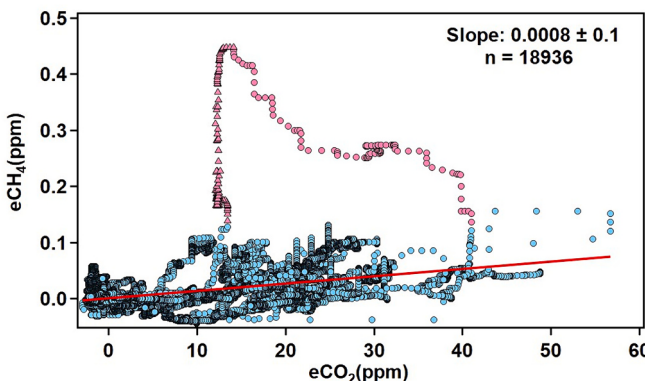


**Fig. 4.** Regression analysis of ΔCO<sub>2</sub> and ΔCH<sub>4</sub> in the urban area of Zhengzhou. Red dots represent the outliers from Flight 16 that were not used in the final correlation analysis (triangle dots represent the measurements near the CNG station on Longhai Road while the round dot represents the measurements near the railway station). The slope and the number of data are also shown.

obtained from ground mobile monitoring within the urban area of Beijing during non-winter time, while the ΔCH<sub>4</sub>/ΔCO<sub>2</sub> ratio in urban Beijing during winter time was 0.00001 (Sun et al., 2019).

### 3.2. Spatial autocorrelation

While urban networks have been setup to monitor GHG levels in many cities (Lin et al., 2018; Kim et al., 2018; Müller et al., 2020), few reports are available on their design criteria, in particular those regarding the representativeness of locations for monitoring stations and spatial gap requirements between stations. These design criteria are important for the networks, since they reflect the purposes of the monitoring and determine whether such purposes will be fulfilled. Although many stations are logically and intuitively set up at locations representing influences from nearby or regional sources, most have not been subject to rigorous spatial relationship analyses, and as such their true representativeness may be called into question.

Such issues can be addressed through spatial autocorrelation analyses if given spatially distributed data either from modeling or measurements (Section 2.4). During the study, the UAV's flight speed, which averaged at 11.5 ± 0.5 m/s, was not constant during the flights while the data time stamp was constant at 1 s. As a result, the spatial distance covered in 1 s could vary due to flight speed fluctuations. To address this issue, the recorded measurements were linearly interpolated in space, creating evenly spaced data sequence before calculating the autocorrelation coefficients. After the linear interpolation, the spatial autocorrelation function, which represents the correlation of a variable with a copy of the data itself but spatially shifted, was computed for the new time series of CO<sub>2</sub> and CH<sub>4</sub> mixing ratios across the 16 flights that followed straight paths. The flight paths along the main roads could effectively cover the main urban areas of Zhengzhou, including the city center and the suburbs. Therefore, it's assumed that the spatial autocorrelation is non-directional and can be determined from the sample data collected along these flight paths to represent the spatial autocorrelation of the whole urban area. The resulting autocorrelation coefficients  $r_k$  as well as the confidence intervals are shown in Fig. 5. The approximate 95 % upper and lower confidence bounds are estimated as  $[-2/\sqrt{T}, 2/\sqrt{T}]$ , where T is the sample size. The correlograms in Fig. 5 indicate a consistent and gradual decrease in the autocorrelation coefficients as data spatial distances increase, eventually reaching close to zero.

After a space lag of 0.5 to 3.5 km, the values gradually decreased

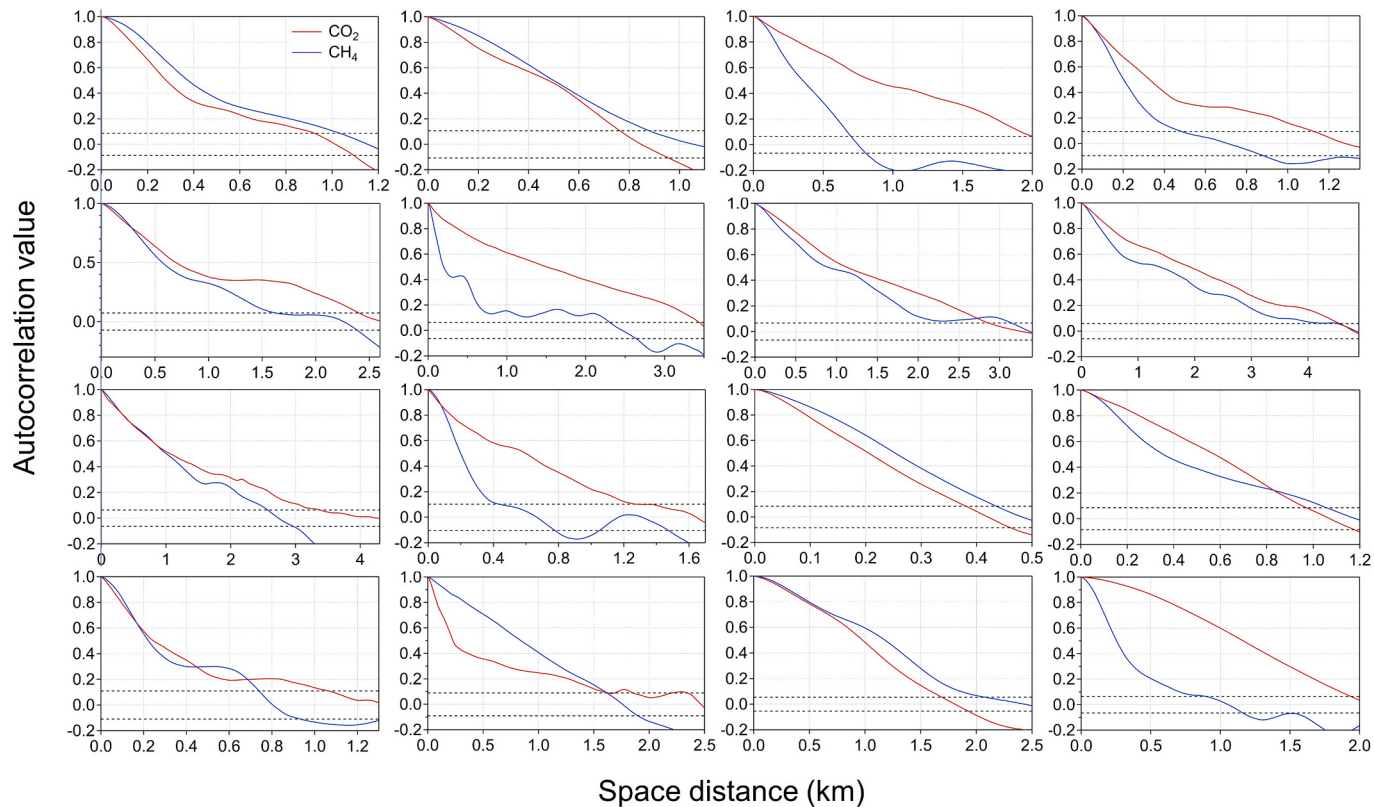


**Fig. 5.** Matrix of  $\text{CO}_2$  and  $\text{CH}_4$  correlogram plots for the 16 flights during the Zhengzhou survey. The blue and red line represent  $\text{CO}_2$  and  $\text{CH}_4$  autocorrelation coefficients decreasing with space distances respectively, the black dash line represents the confidence intervals.

until reaching zero. Fig. 6(a) illustrates the distance lags for both  $\text{CO}_2$  and  $\text{CH}_4$  mixing ratios observed during the flights. The distance lags for  $\text{CO}_2$  and  $\text{CH}_4$  exhibited positive correlations across various flights. This finding suggests that the autocorrelation of a spatial data series, which characterizes the likeness between spatially adjacent observations, is likely independent of the particular gas species being examined. Importantly, the distance lags for both  $\text{CO}_2$  and  $\text{CH}_4$  encompassed a broad range, stretching from distances of under 1 km to 4 km. This indicates that observations taken at spatial scales less than 1–4 km apart have correlation with each other to different degrees. It is noteworthy that for  $\text{CH}_4$ , there are at least 5 flights during which the significant distance lags are around 0.5 km, suggesting that during these flights elevated  $\text{CH}_4$  mixing ratios were highly localized, most likely influenced

by sporadically high emission sources.

It should be noted that both wind directions and wind speeds during the UAV flights are important factors influencing the autocorrelation function and distance lags of the measured mixing ratios. This influence arises from the relative movement between the UAV sampler and the air mass, driven by atmospheric advection. To quantify this relationship, the relative wind speed during the UAV flight is defined as the parallel component of the wind speed minus UAV flying speed:

$$V_{\text{rel}} = V_{\text{wind},\parallel} - V_{\text{UAV}} = V_{\text{wind}} \times \cos\theta - V_{\text{UAV}} \quad (7)$$

where  $V_{\text{rel}}$  is the speed of wind relative to the UAV,  $V_{\text{wind},\parallel}$  is the parallel component of the wind speed,  $V_{\text{UAV}}$  is the UAV ground speed, and  $\theta$  is the angle between wind direction and the UAV heading. The autocorrelation

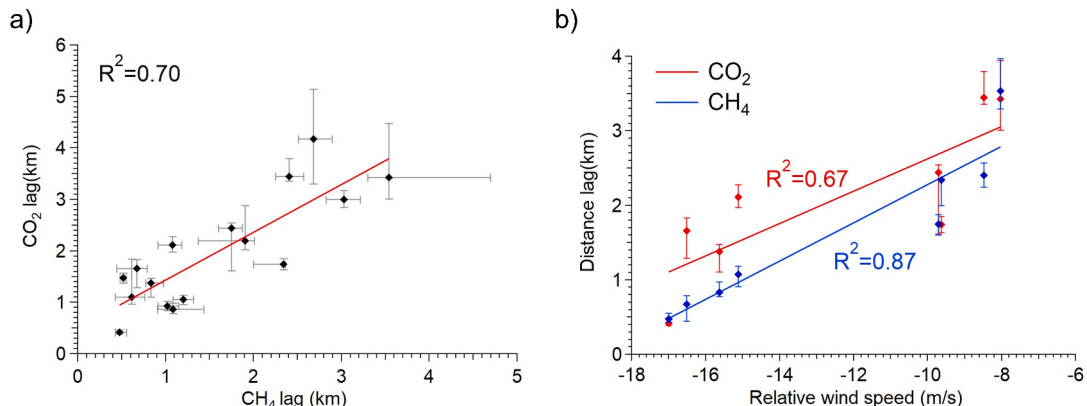


**Fig. 6.** a) The relation between the distance lags of  $\text{CO}_2$  and  $\text{CH}_4$  during different flights, with a coefficient of 0.70. b) The relation between the relative wind speed ( $V_{\text{rel}}$ ) and space lags of  $\text{CO}_2$  and  $\text{CH}_4$ , where the red line and dots represent  $\text{CO}_2$ , and the blue line and dots represent  $\text{CH}_4$ . The coefficient is 0.67 for  $\text{CO}_2$  and 0.87 for  $\text{CH}_4$ .

of CO<sub>2</sub> or CH<sub>4</sub> is associated with the relative wind speed to the UAV heading. Among the six flights where meteorological data were available, the distance lags of CO<sub>2</sub> and CH<sub>4</sub> demonstrated a linear relationship with the relative wind speed ( $r^2 = 0.67$  for CO<sub>2</sub>,  $r^2 = 0.87$  for CH<sub>4</sub>,  $p < 0.001$ , Fig. 6(b)). When the parallel component of the wind speed is equal to zero, the corresponding distance lag signifies the true distance lag unaffected by wind speed and direction. Consequently, the actual spatial extent of autocorrelation is determined to be  $2.3 \pm 1.07$  km for CO<sub>2</sub> and  $1.9 \pm 0.68$  km for CH<sub>4</sub>.

The autocorrelation, with spatial extents of  $2.3 \pm 1.07$  km for CO<sub>2</sub> and  $1.9 \pm 0.68$  km for CH<sub>4</sub>, holds significant implications for monitoring purposes, as they indicate the maximum spatial intervals between nodes in the monitoring network:  $4.6 \pm 2.14$  km for CO<sub>2</sub> and  $3.8 \pm 1.36$  km for CH<sub>4</sub>. The spatial gaps among the different flights ranged from 2 km to 5 km, thereby basically providing sufficiently high spatial resolution for effectively mapping atmospheric CO<sub>2</sub> and CH<sub>4</sub> across the city. However, the distance between the original monitoring sites in Zhengzhou (Fig. 1) spans from 8 km to 15 km. At these distances, variations in both CO<sub>2</sub> and CH<sub>4</sub> across space may only be partially captured directly from the monitoring stations. Consequently, a denser monitoring network is necessary to capture the data needed for inverse modeling aimed at emission determination.

### 3.3. Kriging interpolation estimates

The underlying assumption for Kriging interpolation is that such data spatial distribution shall remain static. In the atmosphere, air parcels move around and therefore violate this assumption. To address this problem, corrections were made for air parcel movement by using concurrent measurements of 3-dimensional wind, so that the geolocation of each air parcel (each data point) is identified for the same point in time. Effectively, such correction “freezes” the geolocation of the air parcel while its CO<sub>2</sub>/CH<sub>4</sub> mixing ratios were measured from the UAV. Before fitting variogram models to the results from the present study and subsequent kriging interpolations, the wind impact was corrected by recalculating the original geolocations of the measured points using the following equations:

$$x'_n = x_n - u_n^*(t_n - t_0) \quad (8)$$

$$y'_n = y_n - v_n^*(t_n - t_0) \quad (9)$$

where  $(x'_n, y'_n)$  represents the original geocoordinates of point  $n$ , while  $(x_n, y_n)$  represent the observed geocoordinates of point  $n$ ,  $u_n$  and  $v_n$  represent the parallel and the normal components of the wind speed along the flight direction, respectively.  $t_n$  and  $t_0$  represent the time in seconds at point  $n$  and the start of the UAV flight, respectively. After the

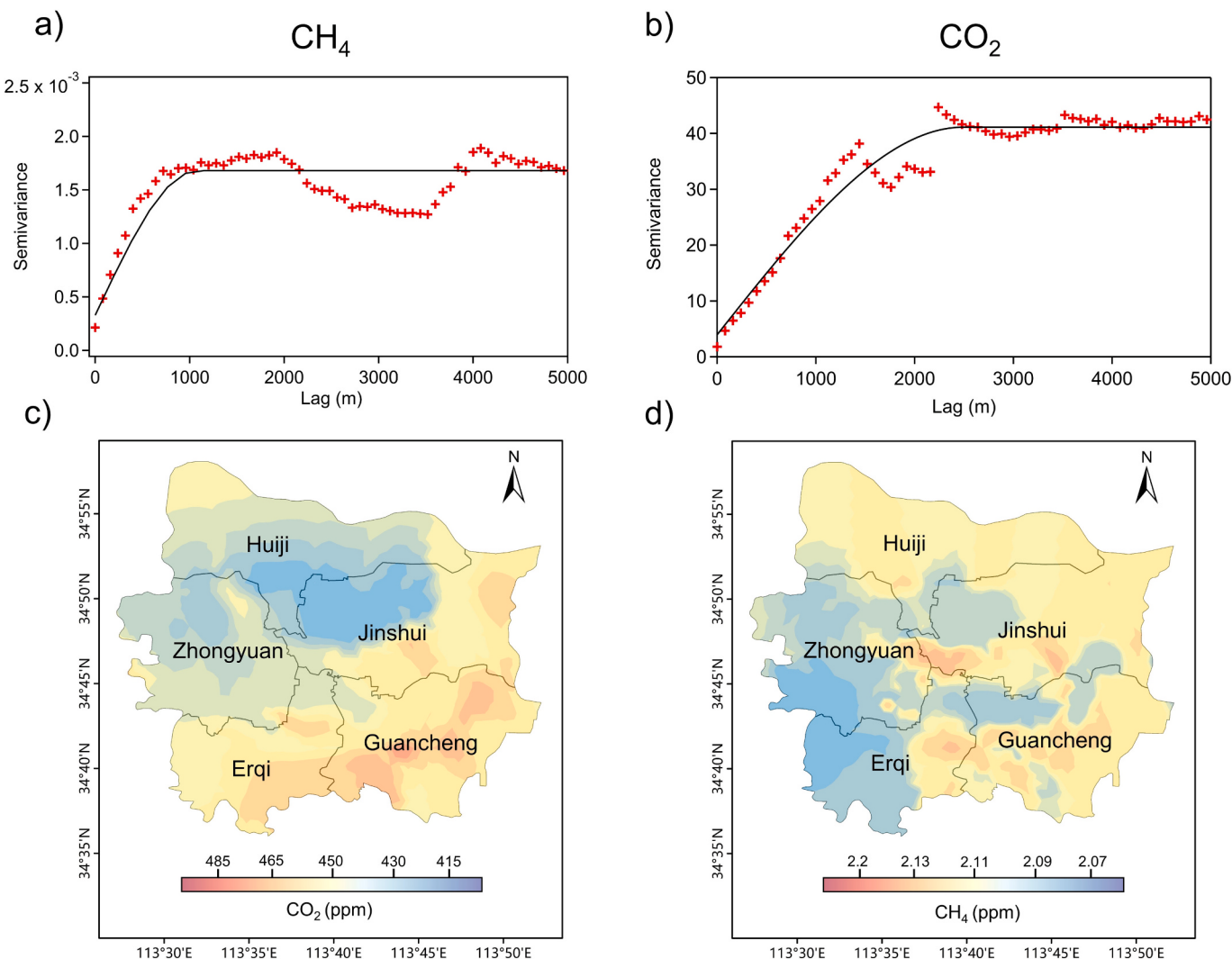


**Fig. 7.** a) and b) Semivariance of CH<sub>4</sub> and CO<sub>2</sub> and their fitted variogram models; c) and d) Image plots of CH<sub>4</sub> and CO<sub>2</sub> mixing ratio predictions over the urban areas of Zhengzhou City using the ordinary kriging method.

geocoordinate corrections of all the observed data points from the 17 UAV flights, the semi-variance of the CO<sub>2</sub> and CH<sub>4</sub> data measured from the UAV is computed, and the associated variogram model is fitted using spherical functions, as shown in Fig. 7 (a) and (b). The specific model parameters (range, sill, and nugget) as well as their standard deviations for both CO<sub>2</sub> and CH<sub>4</sub> data are shown in Table 1. The variogram analysis indicates that as data points draw nearer to each other, the semi-variance reduces. This indicates that the discrepancies between these data points tend to be smaller when they are spatially closer. Conversely, as the distance between data points increases, the semi-variance becomes larger. The range represents the distance where the semi-variance flattens out, indicating a distance beyond which pairs of data points are no longer spatially correlated. Hence, the range parameter determined from the variogram model is an excellent indicator of spatial representativeness of measurements at any single location. As shown in Table 1, the range values for CO<sub>2</sub> and CH<sub>4</sub> are 2.5 ± 0.1 km and 1.1 ± 0.2 km respectively, which is consistent with the distance lags derived based on the previous autocorrelation analysis (2.3 ± 1.07 km for CO<sub>2</sub> and 1.9 ± 0.68 km for CH<sub>4</sub>). Spatial correlation can also be assessed by examining the ratio of nugget to sill, presented as a percentage. Generally, a ratio below 25 % indicates strong spatial correlation. Consequently, it is evident that the observed CO<sub>2</sub> and CH<sub>4</sub> data exhibit a strong spatial correlation, with a nugget to sill ratio of 10.8 % for CO<sub>2</sub> and 15 % for CH<sub>4</sub>, indicating strong spatial correlations within their respective range values.

The levels of CO<sub>2</sub> and CH<sub>4</sub> at unobserved locations across the urban region of Zhengzhou were predicted using the ordinary kriging method. Fig. 7 (c) and (d) illustrate maps depicting the predicted CO<sub>2</sub> and CH<sub>4</sub> mixing ratios, respectively, evaluated on a regular 50 m grid spanning the entire city. It is important to note that the interpolated values for the northernmost district of Huiji should be interpreted with caution due to limited UAV survey coverage in a small portion of the Huiji district. After CO<sub>2</sub> and CH<sub>4</sub> were interpolated at 50 m grid resolution, the interpolated mixing ratios were compared with previous point observations conducted at 1.5 m above the ground at the Henan Academy of Agricultural Sciences (Shi et al., 2013). The CO<sub>2</sub> mixing ratio measured at the monitoring station at 7:00 am in summer was around 400 ppm, while the interpolated value was 410 ppm at the same spot. Despite the two measurements being taken in different years, the UAV-based results are comparable to the observations from other in situ measurements on the ground. Moreover, the GOSAT Level-3 monthly CO<sub>2</sub> and CH<sub>4</sub> column-averaged mixing ratios during June 2022 in the investigated area were obtained from the GOSAT Data Archive Service and compared with the CO<sub>2</sub> and CH<sub>4</sub> values after Kriging from UAV measurements. The satellite-based mixing ratios were 417 ppm for CO<sub>2</sub> and 1.91 ppm for CH<sub>4</sub>, while the average UAV-measured mixing ratios were 454 ppm for CO<sub>2</sub> and 2.12 ppm for CH<sub>4</sub> in Zhengzhou. The difference between UAV and satellite measurements of CO<sub>2</sub> and CH<sub>4</sub> mixing ratios can be attributed to several factors. First, our UAV was operated at 150 m altitudes, allowing them to sample the near-surface layer directly, where CO<sub>2</sub> and CH<sub>4</sub> mixing ratios are often higher due to surface emissions. In contrast, satellites measure column-concentrations, that when converted to concentrations would have averaged mixing ratios that integrate over the assumed mixed layer of the lower atmosphere, resulting in smoothed-out average values and would have lower concentrations than near surface measurements. Second, UAVs provide much higher spatial resolution measurements, capturing fine-scale variations in mixing ratios near the surface, whereas satellites generally have coarser spatial resolution (2.5° × 2.5°), leading to averaged values over larger areas that may dilute the impact of localized high emissions. Third, the GOSAT data were monthly averaged concentrations for June 2022, while the UAV measurements were only conducted for 5 days. Since daily variations can be significant, the specific days chosen for sampling can substantially affect the resulting averages.

Our interpolated mixing ratio maps showing the spatial distribution of GHGs hold particular significance in the process of selecting

**Table 1**

Variogram model parameters for the observed CH<sub>4</sub> and CO<sub>2</sub> mixing ratios.

	Range (m)	Sill	Nugget	Nugget/Sill (%)
CO <sub>2</sub>	2494 ± 109	37 ± 1	4 ± 1	10.8
CH <sub>4</sub>	1078 ± 212	0.002 ± 0.0002	0.0003 ± 0.0002	15

observation sites for GHG monitoring in Zhengzhou. They offer decision-makers valuable insights into the distribution of areas with high, medium, and low mixing ratios of GHGs across the city. These interpolation maps play a vital role in assisting decision-makers in confirming optimal locations for establishing observation stations dedicated to the long-term monitoring of GHGs throughout the urban expanse of Zhengzhou.

#### 4. Conclusion

A UAV-based survey was conducted in the urban region of Zhengzhou, China. The campaign covered a total flight track distance of 170 km, following the city's primary road network. The spatial distributions of CO<sub>2</sub> and CH<sub>4</sub> mixing ratios across the city were analyzed based on spatial autocorrelation and Kriging interpolation of the CO<sub>2</sub> and CH<sub>4</sub> mixing ratios determined from the UAV survey. Results indicate that spatial correlation ranges are approximately 2 km for both CO<sub>2</sub> and CH<sub>4</sub> in Zhengzhou. These spatial correlation ranges, along with the interpolation maps of CO<sub>2</sub> and CH<sub>4</sub> spatial distribution, confirm the siting criteria for the monitoring network being setup for long-term monitoring in the city's urban area. Moreover, the existing GHG monitoring network in Zhengzhou requires additional sites placed at closer intervals. This adjustment is essential to ensure that the spatial gap between monitoring sites is approximately within 4 km, allowing for a representative map of GHG levels across the city. Such enhanced network is crucial in inverse modeling for accurate GHG emission estimation.

#### CRediT authorship contribution statement

Tianran Han: Writing – original draft, Visualization, Methodology, Formal analysis. Conghui Xie: Methodology, Formal analysis. Yanrong Yang: Validation, Methodology. Yuheng Zhang: Validation, Methodology. Yufei Huang: Validation. Yayong Liu: Validation. Keyu Chen: Validation. Haijiong Sun: Validation. Jietao Zhou: Validation. Chang Liu: Validation. Junfei Guo: Validation. Zhijun Wu: Writing – review & editing. Shao-Meng Li: Supervision, Funding acquisition, Conceptualization.

#### Declaration of competing interest

The authors declare that they have no known competing financial interests or personal relationships that could have appeared to influence the work reported in this paper.

#### Data availability

Data will be made available on request.

#### Acknowledgments

This research is supported by the National Natural Science Foundation of China Creative Research Group Fund (grant no. 22221004).

#### References

- Allen, G., Hollingsworth, P., Kabbabe, K., Pitt, J.R., Mead, M.I., Illingworth, S., Roberts, G., Bourn, M., Shallcross, D.E., Percival, C.J., 2019. The development and trial of an unmanned aerial system for the measurement of methane flux from

- landfill and greenhouse gas emission hotspots. *Waste Manag.* 87, 883–892. <https://doi.org/10.1016/j.wasman.2017.12.024>.
- Balling Jr., R.C., Cerveny, R.S., Idso, C.D., 2001. Does the urban CO<sub>2</sub> dome of Phoenix, Arizona contribute to its heat island? *Geophys. Res. Lett.* 28, 4599–4601. <https://doi.org/10.1029/2000GL012632>.
- Barchyn, T.E., Hugenholtz, C.H., Myshak, S., Bauer, J., 2017. A UAV-based system for detecting natural gas leaks. *J. Unmanned Veh. Syst.* 6, 18–30. <https://doi.org/10.1139/juvs-2017-0018>.
- Belkhiri, L., Tiri, A., Mouni, L., 2020. Spatial distribution of the groundwater quality using kriging and co-kriging interpolations. *Groundw. Sustain. Dev.* 11, 100473. <https://doi.org/10.1016/j.gsd.2020.100473>.
- Büns, C., Kuttler, W., 2012. Path-integrated measurements of carbon dioxide in the urban canopy layer. *Atmos. Environ.* 46, 237–247. <https://doi.org/10.1016/j.atmosenv.2011.09.077>.
- Chan, E., Worthy, D.E.J., Chan, D., Ishizawa, M., Moran, M.D., Delcloo, A., Vogel, F., 2020. Eight-year estimates of methane emissions from oil and gas operations in Western Canada are nearly twice those reported in inventories. *Environ. Sci. Technol.* 54, 14899–14909. <https://doi.org/10.1021/acs.est.0c04117>.
- Davis, J.C., Sampson, R.J., 1986. *Statistics and Data Analysis in Geology*. Wiley, New York.
- Defrattyka, S.M., Paris, J.D., Yver-Kwok, C., Fernandez, J.M., Korben, P., Bousquet, P., 2021. Mapping urban methane sources in Paris, France. *Environ. Sci. Technol.* 55, 8583–8591. <https://doi.org/10.1021/acs.est.1c00859>.
- George, K., Ziska, L.H., Bunce, J.A., Quebedeaux, B., 2007. Elevated atmospheric CO<sub>2</sub> concentration and temperature across an urban-rural transect. *Atmos. Environ.* 41, 7654–7665. <https://doi.org/10.1016/j.atmosenv.2007.08.018>.
- Golston, L., Aubut, N., Frish, M., Yang, S., Talbot, R., Gretencord, C., McSpiritt, J., Zondlo, M., 2018. Natural gas fugitive leak detection using an unmanned aerial vehicle: localization and quantification of emission rate. *Atmosphere* 9. <https://doi.org/10.3390/atmos09090333>.
- Gratani, L., Varone, L., 2005. Daily and seasonal variation of CO<sub>2</sub> in the city of Rome in relationship with the traffic volume. *Atmos. Environ.* 39, 2619–2624. <https://doi.org/10.1016/j.atmosenv.2005.01.013>.
- Ha, H., Olson, J.R., Bian, L., Rogerson, P.A., 2014. Analysis of heavy metal sources in soil using kriging interpolation on principal components. *Environ. Sci. Technol.* 48, 4999–5007. <https://doi.org/10.1021/es405083f>.
- Han, T., Xie, C., Liu, Y., Yang, Y., Zhang, Y., Huang, Y., Gao, X., Zhang, X., Bao, F., Li, S.-M., 2024. Development of a continuous UAV-mounted air sampler and application to the quantification of CO<sub>2</sub> and CH<sub>4</sub> emissions from a major coking plant. *Atmos. Meas. Tech.* 17, 677–691. <https://doi.org/10.5194/amt-17-677-2024>.
- Haszpra, L., Barcza, Z., Hidy, D., Szilágyi, I., Dlugokencky, E., Tans, P., 2008. Trends and temporal variations of major greenhouse gases at a rural site in Central Europe. *Atmos. Environ.* 42, 8707–8716. <https://doi.org/10.1016/j.atmosenv.2008.09.012>.
- He, Z., Lei, L., Zhang, Y., Sheng, M., Wu, C., Li, L., Zeng, Z.-C., Welp, L.R., 2020. Spatio-temporal mapping of multi-satellite observed column atmospheric CO<sub>2</sub> using precision-weighted kriging method. *Remote Sens.* 12, 576. <https://doi.org/10.3390/rs12030576>.
- Henninger, S., Kuttler, W., 2010. Near surface carbon dioxide within the urban area of Essen, Germany. *Phys. Chem. Earth A/B/C* 35, 76–84. <https://doi.org/10.1016/j.pce.2010.03.006>.
- Idso, C.D., Idso, S.B., Balling Jr., R.C., 2001. An intensive two-week study of an urban CO<sub>2</sub> dome in Phoenix, Arizona, USA. *Atmos. Environ.* 35, 995–1000. [https://doi.org/10.1016/S1352-2310\(00\)00412-X](https://doi.org/10.1016/S1352-2310(00)00412-X).
- IPCC, 2022. Summary for Policy Makers in Climate Change 2022: Mitigation of Climate Change. Contribution of Working Group III to the Sixth Assessment Report of the Intergovernmental Panel on Climate Change. Cambridge University Press, Cambridge, United Kingdom and New York, NY, USA.
- Jackson, R.B., Saunois, M., Bousquet, P., Canadell, J.G., Poulter, B., Stavert, A.R., Bergamaschi, P., Niwa, Y., Segers, A., Tsuruta, A., 2020. Increasing anthropogenic methane emissions arise equally from agricultural and fossil fuel sources. *Environ. Res. Lett.* 15, 071002. <https://doi.org/10.1088/1748-9326/ab9ed2>.
- Kim, J., Shusteron, A.A., Lieschke, K.J., Newman, C., Cohen, R.C., 2018. The Berkeley atmospheric CO<sub>2</sub> observation network: field calibration and evaluation of low-cost air quality sensors. *Atmos. Meas. Tech.* 11, 1937–1946. <https://doi.org/10.5194/amt-11-1937-2018>.
- Lan, X., Thoning, K.W., Dlugokencky, E.J., 2024. Trends in Globally-averaged CH<sub>4</sub>, N<sub>2</sub>O, and SF<sub>6</sub> Determined From NOAA Global Monitoring Laboratory Measurements. Version 2024-04. <https://doi.org/10.15138/P8XG-AA10>.
- Lee, H., Han, S.-O., Ryoo, S.-B., Lee, J.-s., Lee, G.-w., 2018. The measurement of atmospheric CO<sub>2</sub> at KMA/GAW regional stations, the characteristics, and comparisons with other East Asian sites. *Atmos. Chem. Phys. Discuss.* 19, 2149–2163. <https://doi.org/10.5194/acp-2018-886>.
- Lin, J.C., Mitchell, L., Crosman, E., Mendoza, D.L., Buchert, M., Bares, R., Fasoli, B., Bowling, D.R., Pataki, D., Catharine, D., 2018. CO<sub>2</sub> and carbon emissions from cities: linkages to air quality, socioeconomic activity, and stakeholders in the Salt Lake City urban area. *Bull. Am. Meteorol. Soc.* 99, 2325–2339. <https://doi.org/10.1175/BAMS-D-17-0037.1>.
- Liu, M., Meng, Z., She, Q., Zhu, X., Wei, N., Peng, X., Xu, Q., 2019. Spatial variability and determinants of atmospheric methane concentrations in the metropolitan city of Shanghai, China. *Atmos. Environ.* 214, 116834. <https://doi.org/10.1016/j.atmosenv.2019.116834>.
- Mallia, D.V., Mitchell, L.E., Kunik, L., Fasoli, B., Bares, R., Gurney, K.R., Mendoza, D.L., Lin, J.C., 2020. Constraining urban CO<sub>(2)</sub> emissions using mobile observations from a light rail public transit platform. *Environ. Sci. Technol.* 54, 15613–15621. <https://doi.org/10.1021/acs.est.0c04388>.
- Mayer, S., Sandvik, A., Jonassen, M.O., Reuder, J., 2010. Atmospheric profiling with the UAS SUMO: a new perspective for the evaluation of fine-scale atmospheric models. *Meteorol. Atmos. Phys.* 116, 15–26. <https://doi.org/10.1007/s00703-010-0063-2>.
- Metya, A., Datye, A., Chakraborty, S., Tiwari, Y.K., Sarma, D., Bora, A., Gogoi, N., 2021. Diurnal and seasonal variability of CO<sub>2</sub> and CH<sub>4</sub> concentration in a semi-urban environment of western India. *Sci. Rep.* 11, 2931. <https://doi.org/10.1038/s41598-021-82321-1>.
- Mitchell, L.E., Crosman, E.T., Jacques, A.A., Fasoli, B., Leclair-Marzolf, L., Horel, J., Bowling, D.R., Ehleringer, J.R., Lin, J.C., 2018. Monitoring of greenhouse gases and pollutants across an urban area using a light-rail public transit platform. *Atmos. Environ.* 187, 9–23. <https://doi.org/10.1016/j.atmosenv.2018.05.044>.
- Müller, M., Graf, P., Meyer, J., Pentina, A., Brunner, D., Perez-Cruz, F., Hüglin, C., Emmenegger, L., 2020. Integration and calibration of non-dispersive infrared (NDIR) CO<sub>2</sub> low-cost sensors and their operation in a sensor network covering Switzerland. *Atmos. Meas. Tech.* 13, 3815–3834. <https://doi.org/10.5194/amt-13-3815-2020>.
- Sahay, S., Ghosh, C., 2012. Monitoring variation in greenhouse gases concentration in urban environment of Delhi. *Environ. Monit. Assess.* 185, 123–142. <https://doi.org/10.1007/s10661-012-2538-8>.
- Sampson, P.D., Richards, M., Szpiro, A.A., Bergen, S., Sheppard, L., Larson, T.V., Kaufman, J.D., 2013. A regionalized national universal kriging model using Partial Least Squares regression for estimating annual PM(2.5) concentrations in epidemiology. *Atmos. Environ.* 75, 383–392. <https://doi.org/10.1016/j.atmosenv.2013.04.015>.
- Shi, L., Lou, Y., Fang, W., 2013. Analysis of change characteristics and influence factor of atmospheric CO<sub>2</sub> concentration in Zhengzhou urban area. *Meteorol. Environ. Sci.* 36, 40–43. <https://doi.org/10.16765/j.cnki.1673-7148.2013.01.004>.
- South China Morning Post, 2022. China's urbanisation growth rate slows to quarter-century low. <https://www.scmp.com/economy/china-economy/article/3168678/chinas-urbanisation-push-could-be-bottleneck-slowest>. Last access: 2022-04-21.
- Sun, W., Deng, L., Wu, G., Wu, L., Han, P., Miao, Y., Yao, B., 2019. Atmospheric monitoring of methane in Beijing using a mobile observatory. *Atmosphere* 10, 554. <https://doi.org/10.3390/atmos10090554>.
- Turner, A.J., Kim, J., Fitzmaurice, H., Newman, C., Worthington, K., Chan, K., Woolridge, P.J., Köehler, P., Frankenberger, C., Cohen, R.C., 2020. Observed impacts of COVID-19 on urban CO<sub>2</sub> emissions. *Geophys. Res. Lett.* 47, e2020GL090037. <https://doi.org/10.1029/2020GL090037>.
- van Zoest, V., Osei, F.B., Hoek, G., Stein, A., 2019. Spatio-temporal regression kriging for modelling urban NO<sub>2</sub> concentrations. *Int. J. Geogr. Inf. Sci.* 34, 851–865. <https://doi.org/10.1080/13658816.2019.1667501>.
- Venturi, S., Tassi, F., Cabassi, J., Gioli, B., Baronti, S., Vaselli, O., Caponi, C., Vagnoli, C., Picchi, G., Zaldei, A., Magi, F., Miglietta, F., Capecciacci, F., 2020. Seasonal and diurnal variations of greenhouse gases in Florence (Italy): inferring sources and sinks from carbon isotopic ratios. *Sci. Total Environ.* 698, 134245. <https://doi.org/10.1016/j.scitotenv.2019.134245>.
- Villa, T.F., Gonzalez, F., Milijevic, B., Ristovski, Z.D., Morawska, L., 2016. An overview of small unmanned aerial vehicles for air quality measurements: present applications and future prospectives. *Sensors* 16, 1072. <https://doi.org/10.3390/s16071072>.
- Wang, P., Zhou, W., Niu, Z., Xiong, X., Wu, S., Cheng, P., Hou, Y., Lu, X., Du, H., 2021. Spatio-temporal variability of atmospheric CO<sub>2</sub> and its main causes: a case study in Xi'an city, China. *Atmos. Res.* 249, 105346. <https://doi.org/10.1016/j.atmos.2020.105346>.
- Wei, C., Wang, M., Fu, Q., Dai, C., Huang, R., Bao, Q., 2020. Temporal characteristics of greenhouse gases (CO<sub>2</sub> and CH<sub>4</sub>) in the megacity Shanghai, China: association with air pollutants and meteorological conditions. *Atmos. Res.* 235, 104759. <https://doi.org/10.1016/j.atmosres.2019.104759>.
- Yang, Y., Zhang, Y., Han, T., Xie, C., Liu, Y., Huang, Y., Zhou, J., Sun, H., Zhao, D., Zhang, K., 2024a. A correction algorithm for propeller-induced airflow and flight attitude changes during three-dimensional wind speed measurements made from a rotary unmanned aerial vehicle. *Atmos. Meas. Tech. Discuss.* 2024, 1–21. <https://doi.org/10.5194/amt-2024-1>.
- Yang, Y., Zhou, J., Xie, C., Tian, W., Xue, M., Han, T., Chen, K., Zhang, Y., Liu, Y., Huang, Y., 2024b. A new methodology for high spatiotemporal resolution measurements of air volatile organic compounds: from sampling to data deconvolution. *Environ. Sci. Technol.* 58 (28), 12488–12497. <https://doi.org/10.1021/es506714h>.
- Ye, S., Chen, Y., Fang, S., Zhang, X., Lu, Y., Lan, W., Zang, K., Zhou, M., Lin, Y., Liu, S., Guo, N., 2024. Analysis of the variation characteristics and influencing factors of atmospheric CO<sub>2</sub> and CH<sub>4</sub> concentrations in Suzhou, China. *Acta Sci. Circumst.* 44, 384–398. <https://doi.org/10.13671/j.hjkxxb.2024.0034>.